Unused to useful: recycling plasma chamber coated waste composite of ZnO and α-Fe2O3 into an active material for sustainable waste-water treatment

Boris Wareppam, N. Joseph Singh, Soumee Chakraborty, Ng. Aomoa, M. Kakati, A. C. de Oliveira, V. K. Garg, K. Priyananda Singh, Suelen Barg, Subrata Ghosh, L. Herojit Singh

Unused to useful: Recycling plasma chamber coated waste composite of ZnO and α-Fe$_2$O$_3$ into an active material for sustainable waste-water treatment

Boris Wareppam[a], N. Joseph Singh[a], Soumee Chakraborty[b], Ng. Aomoa[c,d], M. Kakati[d], A.C. de Oliveira[e], V.K. Garg[e], K. Priyananda Singh[a], Suelen Barg[f], Subrata Ghosh[f,*], L. Herojit Singh[a,*]

[a] Department of Physics, National Institute of Technology Manipur, Langol 795004, India
[b] Materials Science Group, Indira Gandhi Centre for Atomic Research, Kalpakkam 603102, India
[c] Department of Physics, Assam Don Bosco University, Sonapur 782402, Assam, India
[d] CIMPLE-PSI Laboratory, Centre of Plasma Physics-Institute for Plasma Research, Sonapur 782402, Assam, India
[e] Institute of Physics, University of Brasília, 70919-970 Brasília, DF, Brazil
[f] Department of Materials and Henry Royce Institute, School of Natural Sciences, The University of Manchester, Oxford Road, Manchester M13 9PL, United Kingdom

ARTICLE INFO

ABSTRACT

While conventional cleaning to remove the coating from plasma chamber walls becomes essential to reproduce the desired materials on the target substrate for widespread applications, an attention towards wall-deposited materials is scarce. Recycling those waste materials to value-added product is of great importance for sustainable progress of our modern society. Herein, we investigated the materials deposited on the wall of plasma chamber, explored their promising features and compared them with conventionally grown materials. A mixture of ZnO and α-Fe$_2$O$_3$ (ZF) exposed to high energy plasma was collected from the wall (ZF-W) and also from the substrate (ZF-S) to check the feasibility of providing same quality products. With same lattice constant of hematite, magnetite and zinc ferrites, ZF-W differs from ZF-S in coercivity, saturation magnetization, ferromagnetic stoichiometry and defects. In addition, degradation of Methyl Blue (MB) dye in ZF-W without use of any external light sources are comparable, more stable and durable in comparison to ZF-S. The slight differences obtained in the property-performances between ZF-W and ZF-S are attributed to the cationic arrangement and the oxygen vacancy defects present in the structure. The study reflects the potentiality of ZF-W as a promising active material for wastewater treatment just as one can use ZF-S. These findings clearly depict that the unused products with altered intrinsic properties obtained after plasma treatment has similar or even better potential to its actual targeted product and thus can be utilized properly thereby saving cost and time and, hence generates an unexplored direction for the materials science community.

Introduction

Advances in materials have accelerated the development of today's technology and hence enhanced the modern lifestyle of human beings [1,2]. In this context, the technology of deposition methodology becomes indispensable for engineering the advanced materials. Thin-film deposition technique is one of the most popular among them to grow materials with tuneable geometry and structural properties. In the methodology of thin film deposition, mostly substrates are used to grow a desired nanostructure. Amongst, plasma-based deposition technique is well known to synthesize the nanostructures with tuneable geometry and the synthesis can be done at low temperature and faster rate [3–5].

For instant, a high throughput nanowire and nanoparticles production are obtained in gas phase using a microwave plasma jet reactor [6]. In this method, metal powders are poured directly into the plasma cavity and allowed to flow down and the resulting powders are collected either in quartz flask or filter bag at the bottom. However, it is well-known to the material scientists that the coating of the materials on the wall of deposition units are unavoidable during the desired material synthesis. In most of the cases, deposition units get cleaned routinely by conventional approaches to get uniform and reproducible structures on the substrate. For example, oxygen plasma cleaning is the most popular strategy for the nanocarbons growth in plasma chemical vapour depositions [7]. These wall cleaning procedures reflect that the coatings on

the deposition wall never receives an attention either by academic or by the industrial community. Moreover, the use of discarded materials is cost-effective, time saving, sustainable and also increases the resource recovery. The quest of our present research to be addressed here is the capability of those unused materials for potential applications? If they are useful, how they compete with the properties-performances of the materials conventionally grown on the substrates?

In the context of potential applications of advanced materials, environmental pollution is one of the biggest concerns in the current century. Amidst, wastewater treatment is highly essential to get rid of the organic pollutants and dyes from the textile industry, pharmaceutical industry etc. In this regards, plasma assisted reactors have been shown to be very effective in wastewater treatment [8]. Catalyst and plasma reactor is one such reactor where a catalyst and a non thermal plasma are used to remove pollutants from the water bodies [8]. Wang et al. [9] reported a gas phase surface discharge plasma system with the help of activated carbon to treat contamination in water. Also, plasma assisted Fe based metal-organic framework synthesis has been shown to be successful and effective in high adsorption of dye pollutants in water [10]. In this perspective, metal oxide-based materials are found to be promising candidates [11,12,13]. ZnO is well-known photocatalyst under UV irradiation alone whereas spinel ferrites are superb photocatalyst under both visible and UV irradiation. More importantly, spinel ferrite possesses superior magnetic properties, simple composition, abundance, high adsorption and high surface to volume ratio [14]. In order to obtain synergistic effect, metal oxide composites have been prepared and found to exhibit superior properties than its individual counterpart. For example, the degradation of malachite green in ternary spinel composites $Fe_2O_3/ZnFe_2O_4/ZnO$ (99%) is found to be more effective than α-Fe_2O_3 (81%) in visible light due to the formation of hetero-nanostructure with cascading electron transfer which gives high surface area, reduced band gap and ease of generation of electron-hole pair [15]. Hence, ZnO and α-Fe_2O_3 are chosen to synthesis the metal oxide composite in this study. Although degradation of organic dyes under light irradiation with the metal oxides and spinel ferrites have been discussed frequently, artificial UV and visible light source are expensive and not reliable under certain circumstances [16]. Also, UV light component from the sunlight is relatively very low. Thus, a more easy and feasible way to degrade organic dyes is highly desirable without using any light source and external components which is another important focus of the present study.

Herein, we presented an adoptable strategy to prepare mixed metal oxide by mixing ZnO and α-Fe_2O_3 with 1:1 molar ratio homogeneously and exposing it to high-density DC thermal plasma torch at the pressure of 10^{-3} mbar. The samples after exposing to the plasma were unavoidably deposited on the wall of the plasma chamber (labelled as ZF-W) and collected to use as an active material for wastewater treatment. Crystallographic, structural, optical and magnetic properties of ZF-W are thoroughly investigated and the results are compared with the reference sample (labelled as ZF-S). The reference sample, ZF-S, is directly deposited on the substrate surface. Advantage of implementing this method is to procure products which have the same or better level of effectiveness with the products from the targeted region. In this way, a huge amount of samples can be procured with little effort without the need of extra time which can be utilized in the industrial level. Thus, the variant form of the products with the same composition were investigated in degradation of anionic dye for wastewater treatment.

Experimental

Materials

ZnO was purchased from Oxford Lab Fine Chem Llp, α-Fe_2O_3 was purchased from Sigma-Aldrich, Methyl Blue (MB) and Benzoic acid was purchased from Himedia Pvt. Ltd. All reagents were of analytical grade and were used without further purification. Double Distilled water was used throughout the experiment.

Synthesis of ZnO/Fe₂O₃ composite using plasma treatment

A DC thermal plasma torch which is capable of producing highly dense, stable and homogeneous plasma jets was used for synthesizing the composites as shown in Fig. 1 [17]. The torch consists of a tungsten cathode and a stack of copper ring segment separated by Teflon gaskets and a copper anode, all of which were intensely water-cooled during the experiment. The power source used was a DC thyristor-controlled power supply (200 V/400 A) with a high-frequency igniter. The reactant injection chamber is situated downstream to the plasma torch and the converging nozzle.

Prior to the deposition, the sample collection chamber was pumped down with a rotary vacuum pump to 10^{-3} mbar pressure. The mixture of ZnO and α-Fe_2O_3 with a molar ratio of 1:1 respectively was homogenously mixed using wet ball milling for 1 h. The ball-milled mixture of ZnO and α-Fe_2O_3 was dried at 373 K for 4 h and then subjected to plasma using a powder feeder under Argon gas (99.99% purity and feeding rate of 15 lpm). As-deposited samples were collected from the chamber wall and named as ZF-W. To compare the properties and performances of ZF-W, the samples deposited on the stainless-steel substrate (ZF-S) were also collected and similar systematic investigations were carried out. To ensure the purity of the samples from contamination and reproducibility, the wall and substrate was polished with acetone and alcohol, then followed by SiC sheet rubbing and then again by acetone and alcohol before initiating the synthesis process.

Sample characterization and measurements

Morphology and structural characterization of the powder were carried out using JEOL Transmission Electron Microscope (TEM) (JEM-2100) with a 0.19 nm point to point resolution operated at 200 keV. Phase and crystallographic information of the plasma-treated powders were evaluated using X-ray diffraction (XRD) (Bruker-D8 advance-USA) with Cu K_α radiation of wavelength 1.54056 Å. Fourier transform infrared spectrometer (FTIR) (Perkin Elmer-USA) and micro-Raman spectrometer (in-Via Renishaw-UK) were employed to investigate the vibrational properties of the composites. The IR spectra were recorded using a KBr beam splitter. For obtaining the Raman spectra, the samples were excited using a 785 nm solid state laser with 20 × objective lens recorded using a cooled CCD detector. The laser power was kept below 1 mW to avoid over-heating of the sample. The Photoluminescence (PL) emission spectra of composites were recorded using HITACHI F-7000 Fluorescence spectrophotometer with a Xe source at an excitation wavelength of 280 nm at room temperature.

The magnetic measurements were carried out using vibrating sample magnetometer (VSM) upto maximum field of + 50 kOe at 300 K. Fe [57] Mössbauer spectroscopy was utilized in transmission mode with an initial activity of 25 mCi (Wissel, Germany).

Degradation of methyl blue dye

The degradation of methyl blue (MB) was recorded using UV–Vis spectrometer (Shimadzu-1800-Japan) under continuous scan. The amount of degradation of MB due to the catalyst is calculated using the relation:

$$\%degradation = \left(1 - \frac{C}{C_0}\right) \times 100 \qquad (1)$$

where C_0 is the initial concentration of the methyl blue, C is the MB concentration at certain time t. In the catalytic degradation, 1 mg of catalyst was added to 4 ml MB solution in Quartz curvette with the initial concentration of 50 ppm at room temperature 296 K. The experiment was performed under static condition with continuous scan for every 50 s in dark condition without exposure to any light source. The initial pH of the MB aqueous solution was found to be 7.0 and there is no change in the observed pH after adding the catalyst. The pseudo second order kinetic model was calculated by using the relation:

$$\frac{1}{C} - \frac{1}{C_0} = Kt \qquad (2)$$

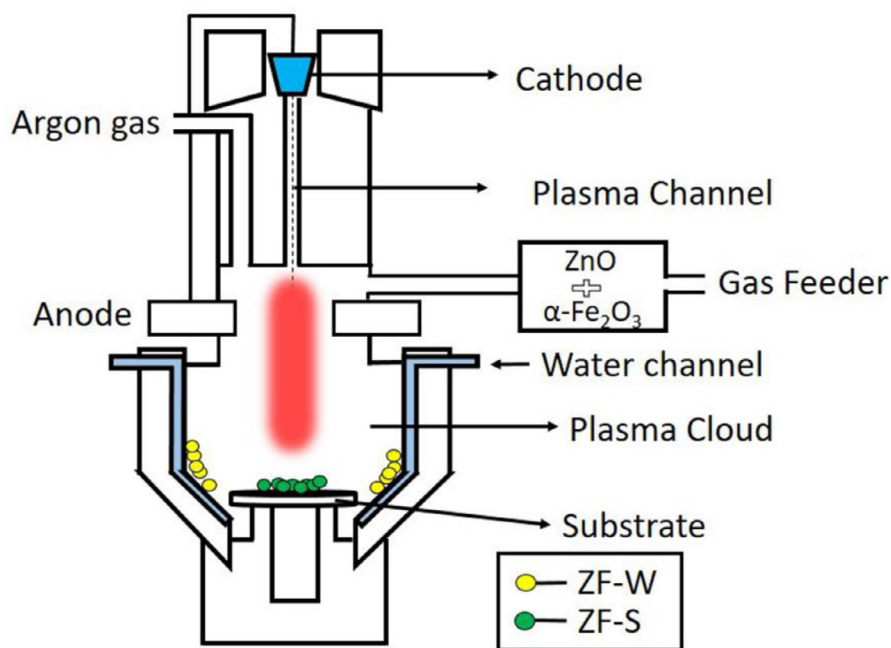Where K is the rate constant in L mg^{-1}min^{-1} and t is the time in min.

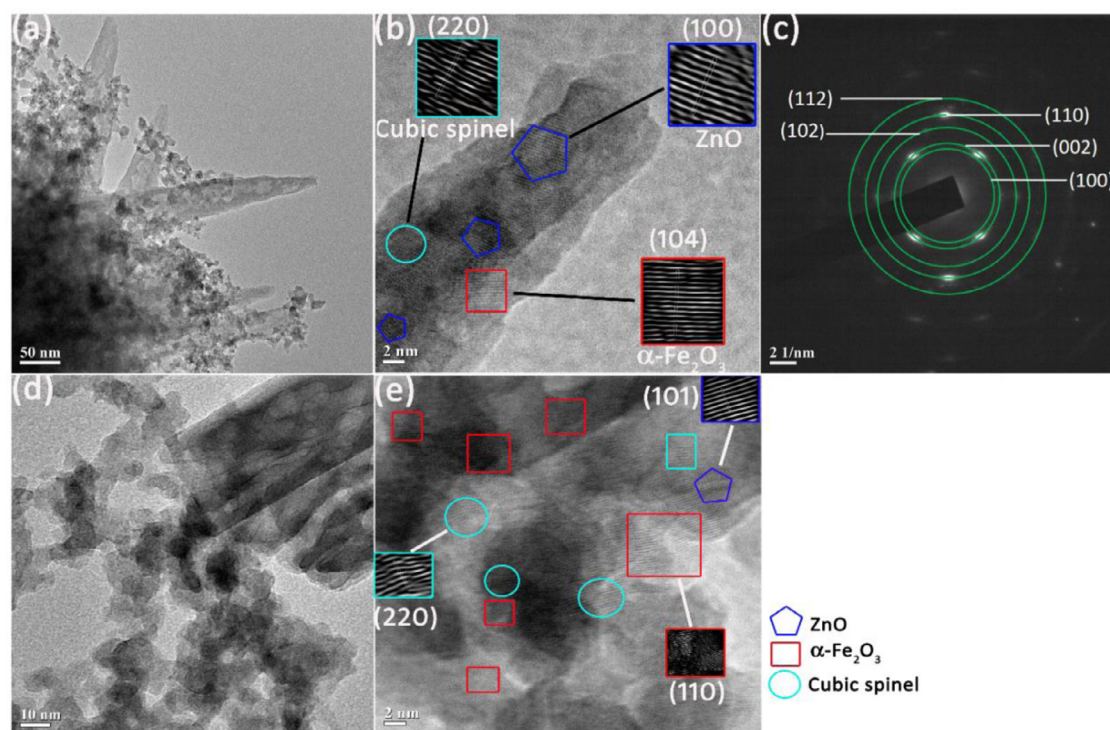**Fig. 1.** Schematic diagram of the DC plasma torch.

Fig. 2. TEM images of (a) ZF-W, (b) rod shaped ZF-W showing the presence of ZnO, inset inverse FFT image of ZnO at (200), α-Fe$_2$O$_3$ at (104) & Cubic spinel at (220) planes (c) SAED pattern of the rod shaped ZF-W, (d) ZF-W at non rod shaped area and (e) ZF-W (at higher magnification 2 nm) showing the presence of ZnO, α-Fe$_2$O$_3$ and Cubic spinel morphologies; inverse FFT image of the selected planes.

Results and discussion

Fundamental analysis

The effect of plasma on the morphology and composition of the composites was of interest. HRTEM images of ZF-W is shown in Fig. 2. Rod shaped structure along with other agglomerated particles were observed Fig. 2(a–d). The high-resolution image (Fig. 2(b)) shows two different contrast region with dark portion at the center of the rod. The inverse

FFT of the selected regions, the corresponding planes obtained from the central portion of the nanorod structure are found to be (102), (104) and (220) of ZnO while the edges represents α-Fe$_2$O$_3$ and cubic spinel ferrites. The SAED obtained on the rods can be marked to (100), (002), (102), (110) and (112) planes of ZnO. From the TEM image, the formation of core-shell structure is depicted. Further, the inverse FFT image highlighted in inset Fig. 2(b) and (e) also gives insight to the distortion in lattice planes which is believe to be caused by the dislocation or defects present in the sample. The impact of defects on the optical
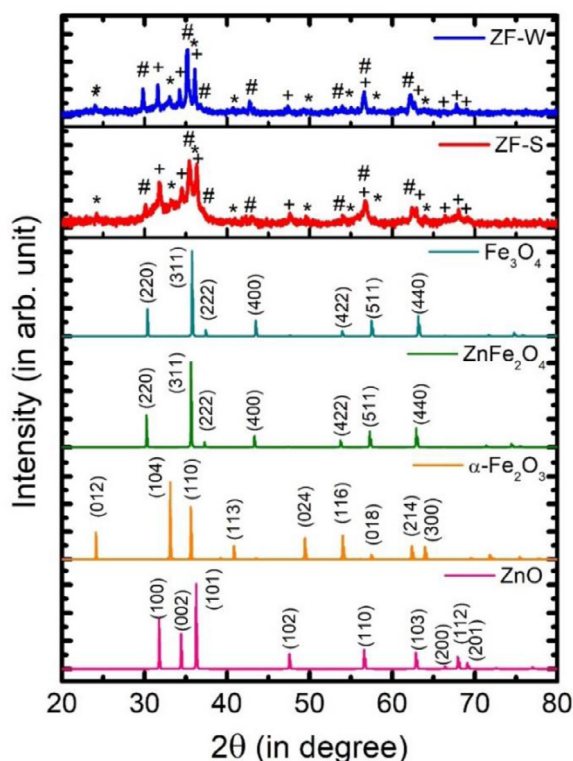
Fig. 3. XRD patterns of ZF-S and ZF-W. The PCPDF patterns of the component materials are provided for comparison. (Assigned) $+ \rightarrow$ ZnO, $* \rightarrow \alpha\text{-Fe}_2\text{O}_3$, $\# \rightarrow$ cubic spinel (ZnFe$_2$O$_4$/Fe$_3$O$_4$).

and magnetic properties shall be discussed in details from PL, Raman spectroscopy, Magnetization and Mössbauer spectroscopy.

To check the integrity of the structural and phase transformation, the structure and phase of plasma-treated metal oxide composites are identified from the X-ray diffractograms. As seen in Fig. 3, the presence of ZnO phase and spinel ferrites (hematite, magnetite and zinc ferrite) are confirmed in both ZF-W and ZF-S. There are no major changes observed in the obtained lattice parameters (Table S1 of Supplementary Information). However, there is slight variation observed in the lattice constants of ZF-S which might have resulted from the intrinsic point defects develop during the synthesis process. The quantification of each component in both samples was estimated using Match software through Rietveld refinement analysis (Fig. S1 of Supplementary Information). It shows that ZF-W consists of 24% ZnO, 30% α-Fe$_2$O$_3$ and 46% cubic spinel ferrites, while ZF-S consist of 37% ZnO, 33% α-Fe$_2$O$_3$ and cubic spinel ferrites of 30%. The formation of cubic spinel ferrites (Fe$_3$O$_4$ and ZnFe$_2$O$_4$) may be attributed to the cationic inter-diffusion of Zn and Fe in the matrix and the induced defect during the plasma treatment. In other words, plasma exposure of mixed metal oxides at high temperature and low pressure generates oxygen vacancies and cationic migration in the matrix. The concept of defect formation and cationic diffusion is clarified from optical and magnetic studies below.

A close inspection of the sample diffractograms in the range of 30–40° shows a broad background representing the presence of amorphous phase in both composites. This amorphous state is found to be much higher in the case of ZF-S than in ZF-W. In fact, the variation in the quantification of XRD data of ZF-S and ZF-W may have been because of this amorphous state that is observed in both the samples. The higher amorphous state in ZF-S may be understood as due to the continuation of cationic migration and reduction of the oxides initiated when exposed to the very high temperature in plasma since the temperature of the substrate is ~973 K. The migration tends to reorganized the lattice resulting to defects whereas in the case of ZF-W, the structural modification and

the atomic states during the exposure to the plasma get freeze as the system get quenched on the wall of the chamber at 278 K. The powder was exposed to the plasma for fraction of seconds and therefore the entire volume of the particle may not be able to achieve the equilibrium temperature and the core of the particles remains unaltered.

As seen in Fig. 4(a) and 4 (b) the PL emission spectra of the both samples comprise of two regions: (i) near band edge emission (NBE) due to excitonic transitions in the UV region (330–410 nm) and (ii) deep-level emission (DLE) arising out of intrinsic defects and extrinsic impurities (410–520 nm) [18,19]. The emission spectra obtained here primarily belong to Zn-site defects and characteristics of the composite since α-Fe$_2$O$_3$ shows fluorescence only in the nano-regime (size less than 20 nm) due to self-trapped states [20]. The observed luminescence profile were deconvulated using Lorentzian line shapes to acquire the peak positions (Fig. 4(a,b)) and the data were extracted in Table S2. A schematic for the PL transition in NBE and DLE are shown in Fig. 4(c). The three emission bands observed at 345 nm (3.59 eV), 383 nm (3.23 eV) and 396 nm (3.13 eV) for ZF-W show resemblance with the previously reported near band edge emission of ZnO (UV region) which is quite close to the band gap energy of ZnO (3.37 eV) [21]. The near band edge emission (NBE) spectra of ZnO is due to free excitonic transitions i.e., the recombination of electrons from the lower edge of the conduction band with the hole present in the highest edge of the valence band. The other region of the emission spectra is contributed by the deep-level emissions which arises due to defects related transitions viz. Zn$_i$ (Zinc interstitial), O$_i$ (Oxygen interstitial), V$_{Zn}$ (Zinc vacancy) and V$_o$ (oxygen vacancy) (see Fig. 4(a) and 4(b). The violet emission spectra observed at 417 nm (2.97 eV) have certain possible transitions to be considered such as Zn$_i$ states trapped at the grain boundary, V$_{Zn}$ vacancy defects, recombination of electrons at Zn$_i$ with the holes of the valence band and transitions related to zinc and Oxygen vacancy defects [18]. Considering the present oxygen-deficient synthesis (i.e. synthesis under inert gas environment), a transition of V$_{Zn}$ and V$_o$ defects seems to be the more plausible reason. The violet emission however may also be due to the transition from ligand to metal charge transfer (LMCT) which is a direct transition [20]. The blue emission spectra in the range 436–453 nm (2.84–2.73 eV) is due to the electronic transitions from Zn$_i$ to valence band and also due to transitions from conduction band to misplaced oxygen defects [22]. The blue emission peak at 468 nm (2.65 eV) is by virtue of the electronic transition from Zn$_i$ to V$_{Zn}$ levels [19]. The green emission band at 492 nm (2.52 eV) in the visible region is because of the combined effect of electronic transition from V$_o$ level and Zn$_i$ to the valence band [22]. PL characteristics similar to ZF-W are observed for ZF-S also. However, a redshift is evidenced in the emission spectra of ZF-S compared to ZF-W. This is due to lower concentration of defect states in the case of ZF-W which may have affected the optical properties of the sample.

The PL peaks were conserved in NBE emission (~ 345, 383 and 396 nm), violet emission (~ 417 nm), blue emission (~ 436, 453, and 468 nm) and green emission (~ 492 nm). These peaks show signature of broadening which is probably due to the structural inhomogeneity present in the both samples (ZF-W and ZF-S) indicating high defect enriched product [23]. Moreover, it is clear from the previous discussions that the contribution of surface oxygen vacancy and defects in ZF-W is less in comparison to ZF-S. An excitonic transition arises due to the presence of oxygen vacancies or defect states. Doping of material can greatly affect the intensity and response range of the PL spectra since it influences the surface oxygen vacancy and defects [24]. The low intensity blue-shifted peak observed at 345 nm for ZF-W as compared to 353 nm for ZF-S is probably due to the excitonic transitions. Higher intensity in ZF-S is because of larger content of surface oxygen vacancies and defects due to the inhibiting effect of Zn^{2+} on the sample. The stronger PL intensity indicates higher probability of exciton occurrence which is provided by the presence of higher surface oxygen vacancies and defects i.e. more oxygen vacancies can bind the electron to form more excitons [25]. However, a stronger PL intensity is observed at 417 nm for ZF-W against 415 nm for ZF-S with a red shift. These are probably transitions
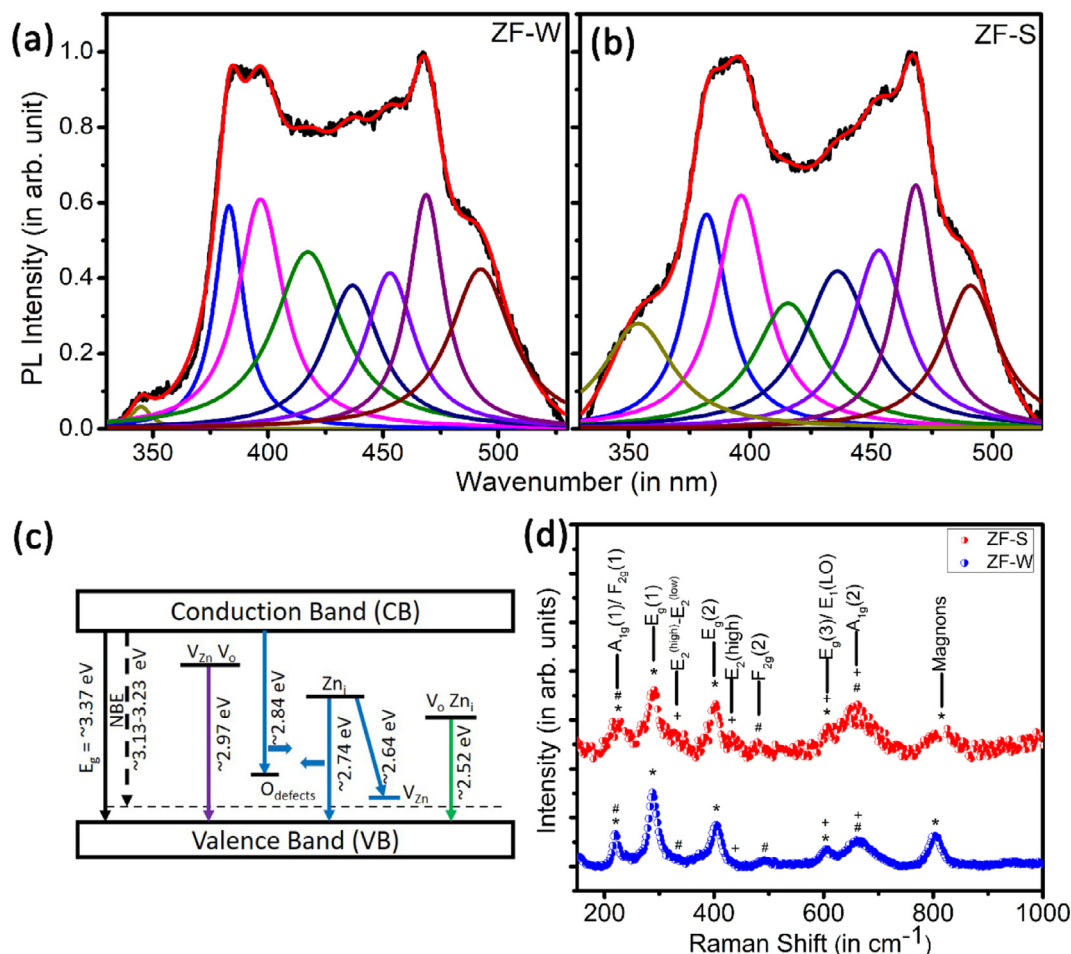
Fig. 4. Photoluminescence emission spectra of (a) ZF-W and (b) ZF-S at room temperature, (c) Schematic diagram of the Photoluminescence transitions in ZF-W and ZF-S and (d) Raman Spectra of ZF-W (blue circles) and ZF-S (red circles). (+ → ZnO, * → α-Fe$_2$O$_3$, # → Cubic Spinel).

from V_{Zn} and V_o as mention earlier. Accordingly, stronger PL intensity means higher content of V_{Zn} and V_o however it is discussed earlier that ZF-S shows more dominance over V_o. Hence, the only plausible reason for showing strong PL spectra in that region is because the V_{Zn} content in ZF-W dominates against that of ZF-S. Thus, the presence of defects states have been confirmed and overall ZF-W has less defect states than ZF-S from the analysis of PL spectra.

Raman Spectroscopy is considered to be a powerful technique to detect crystalline quality, structural defects and disorder in the host lattice [26]. To understand this phenomena, Raman spectra in the range of 190–1000 cm^{-1} is studied. Fig. 4(d) shows the Raman spectra of ZF-W and ZF-S with the corresponding modes assign in Table 1. The Raman spectra were fitted with Lorentzian line shape (Fig. S2 and Table S3). Let us discuss optical phonon mode of α-Fe$_2$O$_3$, ZnFe$_2$O$_4$, Fe$_3$O$_4$ and ZnO individually.

The optical phonon modes of α-Fe$_2$O$_3$ at the Brillouin zone center belong to irreducible representations: $\Gamma_{opt} = 2A_{1g} + 2A_{1u} + 3A_{2g} + 2A_{2u} + 5E_g + 4E_u$ [27] Out of these, $2A_{1g}$ and $5E_g$ are Raman active modes. 220 cm^{-1}(A_{1g}(1)), 288 cm^{-1} (E_g(1)), 403 cm^{-1} (E_g(2)) and 603 cm^{-1} (E_g(3)) are observed for α-Fe$_2$O$_3$ phase of ZF-W. However, it is found that 225 cm^{-1} (A_{1g}(1)), 288 cm^{-1} (E_g(1)), 401 cm^{-1}(E_g(2)) and 606 cm^{-1} (E_g(3)) belongs to α-Fe$_2$O$_3$ phase of ZF-S. Majority of the modes obtained in Raman spectra are of α-Fe$_2$O$_3$ phase which corroborates with the XRD where Fe content is high. Also Raman scattering cross-section is high for α-Fe$_2$O$_3$. Thereafter, we could have two possible contributions for the cubic spinel phase i.e. single phase modes from either ZnFe$_2$O$_4$ or Fe$_3$O$_4$ and the multiphase modes from

the combination of the two. The latter one is more justified for our samples.

The optical phonon modes of ZnFe$_2$O$_4$ at Γ point of the Brillouin zone is represented by $\Gamma_{opt} = A_{1g} + 5E_g + F_{1g} + 3F_{2g} + 2A_u + 2E_u + 4F_{1u} + 2F_{2u}$. [27]. Of which, A_{1g}, E_g and $3F_{2g}$ are the Raman active modes in ZnFe$_2$O$_4$. Similarly, the irreducible representation of phonon modes of Fe$_3$O$_4$ at the zone center is given by $\Gamma_{opt} = A_{1g} + E_g + T_{1g} + 3T_{2g} + 2A_{2u} + 2E_u + 5T_{1u} + 2T_{2u}$. [28] of which A_{1g}, E_g and $3T_{2g}$ are the Raman active modes. 220 cm^{-1}(F_{2g}(1)), 494 cm^{-1}(F_{2g}(2)) and 663 cm^{-1} (A_{1g}(2)) are the modes emerges from ZF-W while 225 cm^{-1} (F_{2g}(1)), 481 cm^{-1} (F_{2g}) and 657 cm^{-1} (A_{1g}(2)) modes were observed for ZF-S. The modes above 600 cm^{-1} are treated as motion of oxygen atoms in tetrahedral AO$_4$ group [27,29]. The A_{1g} modes (663/657 cm^{-1}) which is associated with the vibration of oxygen in the tetrahedral site could also very well be from the Fe$_3$O$_4$ phase. The above vibrational modes are also found for ZnFe$_2$O$_4$ which indicates that overlapping of these vibrational modes are possible [30]. It has been reported that if there are disorders of Zn and Fe cations in the tetrahedral and octahedral sites in the sample, the vibrations related to them will show two separated first-order Raman peaks and modes with very close vibrational frequencies will show overlapped broad peaks with their average value [30]. Likewise, 663/657 cm^{-1} could also be assigned to ZnO E$_1$(LO+TA) multi-phonon modes originated due to disordered modes from the incorporation of other dopant species [31]. However, the contribution from ZnFe$_2$O$_4$ and Fe$_3$O$_4$ seems to be more credible as ZnO modes around this is usually weak. This also explains why 220/225 cm^{-1} modes are assigned for both α-Fe$_2$O$_3$ and ZnFe$_2$O$_4$. These are very

well possible as the prepared samples exist in multiphase as observed from the XRD.

Finally, the optical phonon modes of ZnO is given by $\Gamma_{opt} = A_1 + 2B_1 + E_1 + 2E_2$.. A_1 and E_1 modes are both Raman & IR active whereas E_2 is only Raman active. E_2(low) modes are associated with the non-polar vibration of Zn sub-lattice while E_2(high) modes involves the vibration of lighter oxygen atom [38,39]. Fig. 4(d) depicts the modes of ZnO and the corresponding modes at 327 cm^{-1}(E_2^{high}-E_2^{low}), 434 cm^{-1} (E_2 high) and 603 cm^{-1}(E_1(LO)) are found in ZF-W while 326 cm^{-1}(E_2^{high}-E_2^{low}), 432 cm^{-1} (E_2 high) and 606 cm^{-1}(E_1(LO)) are observed in the case of ZF-S. Here also 603/606 cm^{-1} are assigned to both α-Fe_2O_3 and ZnO similar to earlier case where overlapping of two closed vibrational frequencies giving broad peaks. Surprisingly, E_2(high) mode of ZnO which is usually found to be an intense mode at around 434 cm^{-1} has reduced to a large extent in the case of ZF-W and ZF-S. This may be because of the high content of Fe in the prepared samples ZF-W and ZF-S. It is already reported that higher Fe doping concentration in ZnO matrix leads to decrease in the intensity of E_2(high) modes [26,27,39]. Since E_2(high) mode is associated with the vibration of lighter oxygen atom, diminishing of this peaks suggest that there is lot of oxygen vacant sites due to the reduction at high temperature and low pressure ($\sim 10^{-3}$ mbar). The oxygen atom in the ZnO may have been knocked out due to above said reasons during the plasma treatment which explains the diminishing of E_2(high) mode in the Raman spectra of prepared samples. It seems the local symmetry of the samples (ZF-W and ZF-S) is different from the pure ZnO although the crystal structure is the same which is observed from the XRD. The incorporation of Fe into ZnO can breakdown the translational crystal symmetry and result in disorder-induced suppression of this mode. Furthermore, there is shifting of the vibrational modes in ZF-W and ZF-S. This is attributed to the structural defects and local lattice dislocation induced by the higher incorporation of Fe in the system. The A_1 modes of ZnO are found to be vanishing from the Raman spectra. Similar scenario had been reported by Sahai et al. [27] where 580 cm^{-1}(E_1) and 621 cm^{-1}(A_1) modes disappeared for Fe doped ZnO samples while it appears for the undoped ZnO. This phenomenon is explained as due to alteration of pure ZnO to other phases with Fe incorporation. Furthermore, a relatively higher intense peak at 803 cm^{-1} is observed in ZF-W compared to 817 cm^{-1}. This peak is usually not observed in the Raman spectra of defects-free hematite phase. Although this peak is ignored in some of the reports [40,41], it could be assigned as defected hematite phase [35,42,43] and signifies that the point defects in α-Fe_2O_3 transformed the antiferromagnetic properties to weakly ferrimagnet. Therefore, the peak at $\sim$800 cm^{-1} is understood as the magnon mode of α-Fe_2O_3 as it is also reported by Serreno et al. [37]. Considering the peak at 803 cm^{-1} to be the defected hematite phase, we conclude that the hematite in ZF-W and ZF-S are defected which possesses weak ferromagnetism. Thus, the demarcation of multiphase (ZnO, α-Fe_2O_3, Fe_3O_4 and $ZnFe_2O_4$) from (ZnO + α-Fe_2O_3) which were discussed in XRD and TEM is substantiated from Raman studies.

Since ZnO is diamagnetic and α-Fe_2O_3 is antiferromagnetic in nature, an investigation on the magnetic properties of ZF-W can bring insights on the structural characteristics. A magnetic hysteresis curve was analyzed and it is found that the as-prepared ZF-W is ferromagnetic as shown in Fig. 5(a). Similar observation is also confirmed for ZF-S. Since ZF-W have lower content of ZnO and α-Fe_2O_3 than that of ZF-S (see XRD result), one can expect relatively higher saturation magnetization from ZF-W. Interestingly, the sample ZF-S in spite of having a higher content of ZnO and α-Fe_2O_3 shows a higher saturation magnetization of (51.78 emu/g) than that of the ZF-W (30.93 emu/g). This can be possible if ZF-S composite contains a relatively higher amount of stoichiometric Fe_3O_4 (more accurately $Fe_A/Fe_B \sim 1/2$) or due to defect induced magnetization in ZnO and α-Fe_2O_3. The defect-induced magnetization has been reported for both magnetic and non-magnetic metal oxides [44]. For example, a missing oxygen atom between two adjacent Fe^{3+} atoms on octahedral sites leads to a parallel alignment of Fe mo-

ments and therefore a larger magnetic moment per unit cell [45]. Thus, quantifying Fe_3O_4-content in the composite is necessary to check the possibility of the role of defects in the saturation magnetization of the samples. Towards this, Mössbauer studies were conducted as below. In addition to the saturation magnetization, the coercivity and remanence value of ZF-S are also found to be higher (140.16 Oe and 5.42 emu/g) than ZF-W counterpart (116.39 Oe and 2.94 emu/g) respectively as seen from the inset of Fig. 5(a). These confirm that there is variation in cation distributions in the samples ZF-W and ZF-S.

The clarification in the anomaly with respect to the composition and the magnetization of the ZF-W and ZF-S were carried out using Mössbauer studies (Fig. 5(b)). The extracted parameters are listed in Table 2. Mössbauer analysis of the spectra obtained at room temperature (298 K) of ZF-W shows the presence of 27% α-Fe_2O_3, 22% of octahedral sites (Fe_B) of magnetite and 15% tetrahedral sites exhibiting high quadrupole splitting which may be understood as the intermediate phase of α-Fe_2O_3 and magnetite tending towards α-Fe_2O_3 and 36% of paramagnetic doublet (D). In contrast, ZF-S shows the presence of 18% α-Fe_2O_3, 24% of octahedral sites (Fe_B) & 12% of tetrahedral sites (Fe_A) in Fe_3O_4 and 46% of paramagnetic doublet (D) while quantification from XRD was for the crystalline phases only, Fe [57] Mossbauer spectroscopy identifies both amorphous and crystalline Fe based compounds. Therefore, the deviation in the Mossbauer and XRD data must be due to contribution from the amorphous compounds observed in XRD as broad peaks consisting of cubic spinel ferrites. This good agreement between the two results indicates that the samples collected from the wall are more crystalline.

From Table 2, the average quadrupole splitting of Fe_A and Fe_B ($<\Delta>$) for ZF-W (0.13 mm/s) is found to be higher than ZF-S (0.045 mm/s) where Fe_A and Fe_B represent iron in tetrahedral and octahedral position in spinel ferrites, respectively. More closure $<\Delta>$ value of ZF-S towards zero confirms that the conversion of α-Fe_2O_3 to cubic iron oxide. Moreover, the ratio between Fe_A and Fe_B of 1:2 is a measure of the stoichiometry of ferrimagnetic Fe_3O_4 [46,47]. The deviation of the ratio of Fe content in the tetrahedral and octahedral sites from the ideal ratio of 1:2 also gives us awareness of the presence of vacancies in the octahedral arrangement of the specimens [48]. The ratio between Fe_A and Fe_B of ZF-W and ZF-S are found to be 1.36:2 and 1:2, respectively which confirms the better stoichiometry in ZF-S. Owing to these two reasons, comparatively lower saturation magnetization is observed in ZF-W than ZF-S. The $<\Delta>$ of the paramagnetic doublet of ideal $ZnFe_2O_4$ is $\sim$(0.32–0.39) mm/s [49–52]. However, $<\Delta>$ of the present doublet is 0.41 and 0.53 mm/s for ZF-W and ZF-S respectively which is higher than the ideal $ZnFe_2O_4$. The higher $<\Delta>$ indicates the presence of defects which may be due to oxygen vacancies and cationic disordered arrangement. The Mossbauer spectra of the Fe substituted ZnO is reported to consist of two doublet with $<\Delta>$ of $\sim$0.73 and $\sim$1.53 mm/s [50]. Therefore, in the present sample (ZF-W and ZF-S), Fe doped ZnO is plausibly coexisted along with $ZnFe_2O_4$. The content of Fe doped ZnO is higher in the case of ZF-S as the area and $<\Delta>$ of the doublet increases to 46 and 0.53 mm/s respectively.

Our next step is to probe further insights on the oxygen vacancy defect of ZF-W and ZF-S. While looking back on the synthesis methodology, it is realized that ZF-W is grown at low temperature (277 K) since the wall of the deposition chamber is surrounded by circulated chill water whereas ZF-S (973 K) is grown at high substrate temperature although the main precursors pass through under same plasma environment just before the deposition. To explore the effect of quenching during the growth, the Mössbauer spectra of ZF-S was conducted at the lowest available temperature of 80 K in our set-up. The extracted parameters are listed in Table 2. The reduction in the paramagnetic doublet (D) from 46 to 31% reveals the partial inversion (PI) state of $ZnFe_2O_4$ where fractions of Fe occupy the tetrahedral sites (Table 2). The Fe presence in the tetrahedral sites increases the exchange interaction energy among the tetrahedral to octahedral cations (J_{AB}). Therefore, the Neel temperature of the partially inversed $ZnFe_2O_4$ is shifted above 80 K from 10 K for normal spinel ferrites. Same trends are observed for ZF-W where the
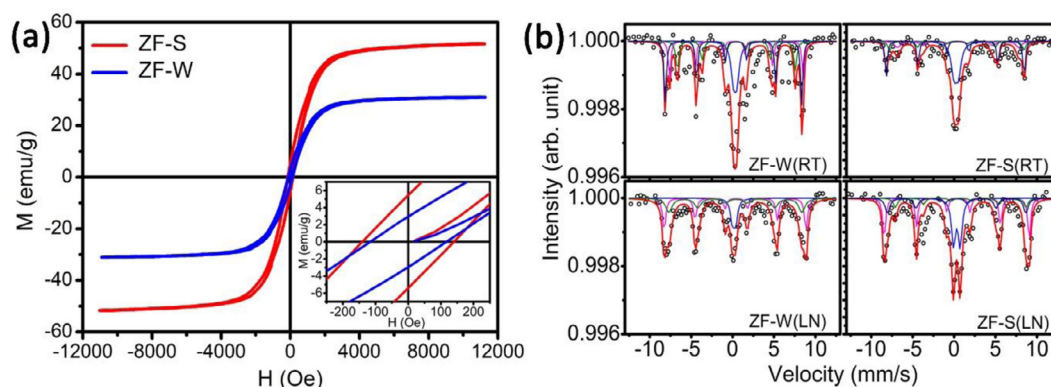
Fig. 5. (a) Magnetic hysteresis curve for the prepared samples. Inset represents a magnified scale of M-H curve to indicate the coercivity of as-grown materials (b) Mössbauer spectra of ZF-W and ZF-S at 298 K (RT) and 80 K (LN).

Table 1

Assignment of Raman modes for ZF-S and ZF-W.

| Phase and bands	Mode wave- number (cm^{-1})		Assignment	Ref.
	ZF-W	ZF-S		
ZnO	327	326	$E_2^{(high)} - E_2^{(low)}$ (Multiphonon modes of ZnO)	[29,32,33]
	434	432	E_2 high mode (Vibration of Oxygen bond)	
α-Fe$_2$O$_3$	288	288	E_g mode vibration of Fe-O bonds	[34,35]
	403	401	E_g mode vibration of oxygen atoms along Fe-O bonds	
Cubic spinel	494	481	A_{1g} (Vibration of Oxygen atom)	[30,36]
Overlapping	220	225	A_{1g} mode of α-Fe$_2$O$_3$ and F_{2g} mode of ZnFe$_2$O$_4$ involves vibration of Fe-O	[34,35,30]
Vibrational modes	603	606	E_g modes of α-Fe$_2$O$_3$ and E_1(LO) modes of ZnO	[29,32,34,35]
	663	657	A_{1g} (ZFO or Fe$_3$O$_4$), disorder-activated mode in ZnO (correspond to symmetric stretching of oxygen atoms along Fe-O bonds)	[30,32,33,36]
Magnon	803	817	Defected hematite phase.	[37]

Table 2

RT Mossbauer data of ZF-S and ZF-W taken at 298 K and 80 K (where the symbols signifies D-Paramagnetic doublet, Fe$_A$- Fe in Tetrahedral Site and Fe$_B$-Fe in Octahedral Site).

Sample /Temperature	Isomer shift (δ in mm/s)	Quadrople splitting (Δ in mm/s)	Mean hyperfine field (B$_{hf}$ in T)	Area (%)	Phase
ZF-W/298 K	0.41(3)	0.41(0)	–	36	D
	0.37(2)	0.32(5)	51.1(0)	27	Fe$_2$O$_3$
	0.42(3)	0.26(8)	50.02(4)	15	Fe$_A$
	0.54(4)	0.009(7)	44.2(3)	22	Fe$_B$
ZF-S/298 K	0.35(3)	0.53(0)	–	46	D
	0.39(2)	0.34(5)	51.7(2)	18	α-Fe$_2$O$_3$
	0.39(1)	0.05(0)	50.3(7)	12	Fe$_A$
	0.56(0)	0.04(0)	45.4(6)	24	Fe$_B$
ZF-W/80 K	0.28(5)	0.41(9)	–	15	D
	0.47(2)	0.13(0)	53.2(2)	31	Intermediate α-Fe$_2$O$_3$ to Fe$_3$O$_4$
	0.48(5)	0.11(9)	49.8(2)	54	
ZF-S/80 K	0.43(3)	0.80(5)	–	31	D
	0.52(3)	0.22(7)	54.3(1)	29	α-Fe$_2$O$_3$
	0.37(8)	0.08(0)	51.8(8)	27	Fe$_A$
	0.92(4)	0.07(0)	48.9(5)	13	Fe$_B$

paramagnetic doublet got reduced from 36 to 15% when the temperature of Mössbauer test is reduced from 300 K to 80 K (Table 2). The quadrupole splitting of sextets for the cubic spinel in ZF-S 80 K is low. So there will be a reduction of Fe^{3+} cation to Fe^{2+} cation with the loss of oxygen. Here, judging from the quadrupole splitting value there is a fractional transformation of hematite to magnetite phase, therefore, further reduction occurred in ZF-S. Whereas the quadrupole splitting of the sextet of ZF-W/80 K is very high from the expected value of cubic spinel. Therefore, a transformation of α-Fe$_2$O$_3$ to Fe$_3$O$_4$ phase could not occur instead they form an intermediate phase of α-Fe$_2$O$_3$ and Fe$_3$O$_4$. Thus, these facts validated that there is a lower amount of oxygen vacancy

defects in the case of the ZF-W. This may have been due to the variation in temperature of the substrate and chiller as the sample collected from the wall (ZF-W) is expected to be quenched. The metal oxides often get reduced or create oxygen vacancies when heated at high temperature in vacuum[53]. In addition to the creation of oxygen vacancies, the cations also migrated at high temperature[54]. The combinational effect of the oxygen vacancies and the motion of cations modifies the structures. The higher saturation magnetization can also be explained as due to the creation of more oxygen vacancy sites and diffusion of cations in the case of ZF-S.
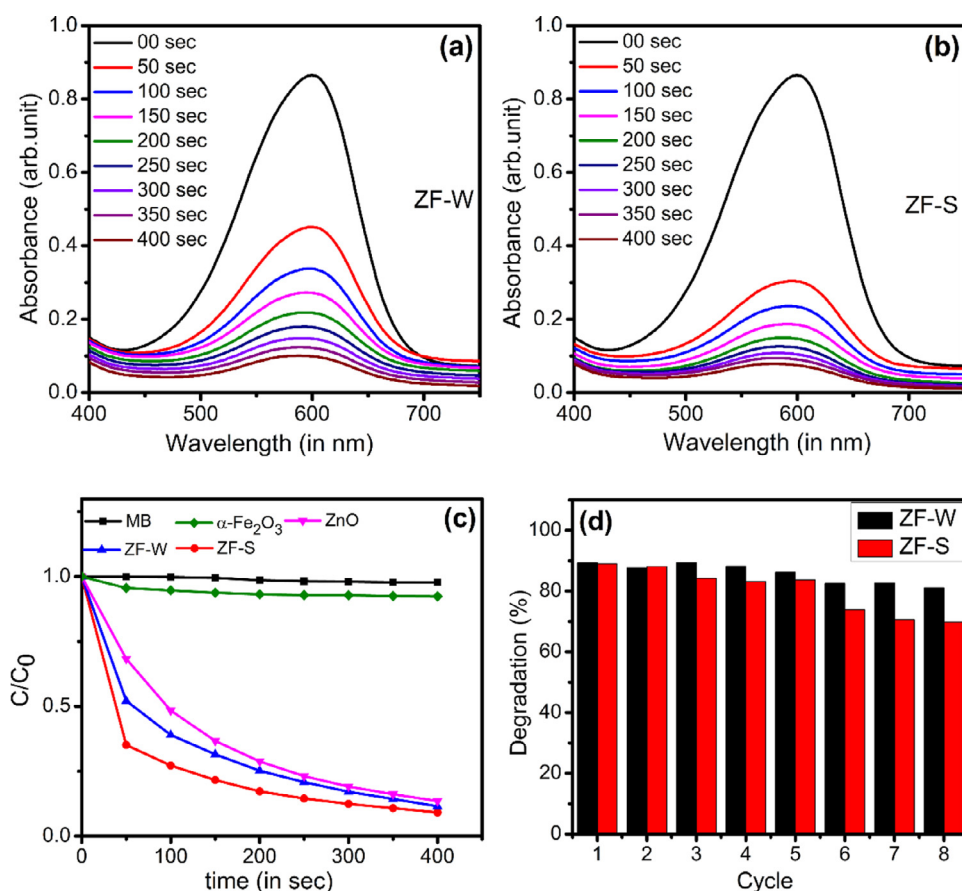
Fig. 6. Reduction of MB dye with (a) ZF-W & (b) ZF-S. (c) Degradation of MB dye over ZF-W and compared with α-Fe$_2$O$_3$, ZnO, and ZF-S. (d) Reusability performance for the sample ZF-W.

Degradation of the methyl blue (MB) dye

Finally, ZF-W is implemented as an active material for dye-adsorption. The degradation of MB dye under reaction with the catalyst ZF-W is shown in Fig. 6(a) which confirms that the degradation occurs very fast and within a very short interval of time. For the sake of comparison, the MB degradation of ZF-S is also shown in Fig. 6(b). The normalized MB degradation of ZF-W over time is estimated using Eq. (1) and shown in Fig. 6(c). It is clear that the MB degradation of ZF-W is comparable with ZF-S and found to be better than ZnO and α-Fe$_2$O$_3$. Pure ZnO acts as a good catalyst in the degradation of MB while there is no significant degradation of MB in the case of α-Fe$_2$O$_3$ as confirmed from Fig. S3 (SI). The faster degradation of an anionic dye in ZnO is already reported as due to the interfacial electron transfer that takes place between donor states (oxygen vacancies and interstitial Zn sites) and MB [55]. Since α-Fe$_2$O$_3$ does not contribute to MB degradation significantly (Fig S3 in SI), the excellent performance of ZF-W and ZF-S than the ZnO catalyst is attributed to the synergistic effect from both oxides. Among the synthesized materials, relatively higher degradation in ZF-S compared to ZF-W (Fig. 6c) can be attributed to the improved charge-transfer capability and surface defects (V_o and V_{Zn}). The oxygen vacancies provide active sites for the redox reaction and create localized state below the conduction band which will lessen the gap between the conduction band and the valence band thus facilitates faster redox reactions. It has been reported in catalytic activities, morphology, surface defects and interface properties plays a crucial role as altering these parameters may affect the recombination rate of electron – hole pair [56]. Moreover, studies have shown that nanorod formation of ZnO with different aspect ratio could modify the rate of separation of these electron and hole pair [57]. Thus, the higher degradation rate could also be contributed by the morphology of the sample (ZF-W and ZF-S) which can be related to the mixed nanorod shaped observed in the HRTEM. However, surface defects would be the main factor leading to degradation of

the MB dye in this case as the prepared samples content large amount of surface defects as conferred earlier. The rate kinetics were also examined using the 2nd order kinetic model (Fig. S4 and Table S4) and it is found that ZF-S and ZF-W have a rate constant of 0.0273 (Lmg^{-1}min^{-1}) and 0.0222 (Lmg^{-1}min^{-1}) respectively which is expected as discussed earlier.

Reusability of the adsorbent is necessary for practical utility and hence further investigation is carried out. The recovered adsorbent were washed thoroughly with distilled water, dried at 65 °C collected and reused. It is shown in Fig. 6(d) that even after repeated cycles the regenerative ability of the prepared sample ZF-W on the removal of MB is quite astonishing. It is observed that the stability of ZF-W is better than ZF-S. Since the samples are magnetic in nature it can be recollected very easily using a magnet.

There are two possible mechanisms involved in the degradation of MB dye in this case: (i) *Reaction with the dye and the catalyst* which gives OH$^\bullet$ radical. The chromophore groups and conjugated systems of anionic dye are destroyed due to oxidation of dye which leads to decolouration;

(ii) *Adsorption of dye due to the catalyst*. Dye molecules can be adsorbed by the metal ions group of the precipitate with the sulfonic group causing decolouration.

To check the possibility of adsorption of MB dye on the surface of the precipitates (ZF-W and ZF-S), the FTIR spectra of the precipitates were taken after the degradation and pure MB (Fig. 7). Analysis of the FTIR spectra shows no attachment of MB dye on the precipitates (ZF-W and ZF-S) taken after the degradation. So, it can be assumed that the dissociation of the dye is more dominant than the adsorption mechanism in our system. The mechanism involved in this degradation process can be explained in terms of oxygen vacancies presence in the sample. The primary step is that the dissociation of water molecules takes place at oxygen vacant sites. When the precipitates interact with water molecules
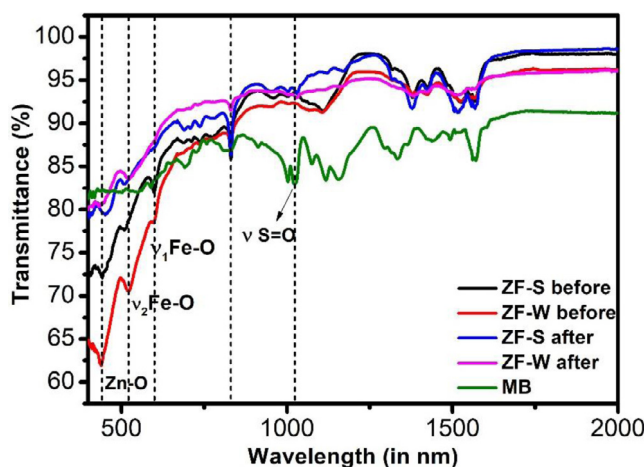
Fig. 7. FTIR spectra of ZF-W and ZF-S before and after the kinetics of MB dye.

(H$_2$O), it splits into hydrogen (H$^\bullet$) radical and hydroxyl (OH $^\bullet$) radical due to the interaction with oxygen vacancies and oxygen atom at the surface of the catalyst as shown in Eq. (3) [58]. The dissociated H$^\bullet$ radical forms another OH$^\bullet$ radical and oxygen (O$^\bullet$) radical with the surface oxygen atom in Eq. (4). The new O$^\bullet$ radical then interacts with other H$_2$O molecules to form two more OH$^\bullet$ radical shown in Eq. (5). These OH$^\bullet$ radical provides oxidation of the MB dye and thus the degradation occurs. The degradation of MB dye due to OH$^\bullet$ radical generation is already reported [59,60]. The generation of OH$^\bullet$ radical was examined by using Benzoic acid which acts as a scavenger for OH$^\bullet$ radical Fig. S5(SI). It was found that the degradation rate of MB was suppressed with the introduction of benzoic acid which confirm the involvement of OH$^\bullet$ radical. This concludes that oxygen vacancies play an important role in the degradation of anionic dye like MB and hence the superiority of degradation in ZF-S than the other is related to the oxygen vacancies.

$$H_2O + O_{vacancy} \rightarrow H^\bullet + OH^\bullet \tag{3}$$

$$H^\bullet + O_2 \rightarrow OH^\bullet + O^\bullet \tag{4}$$

$$O^\bullet + H_2O \rightarrow 2OH^\bullet \tag{5}$$

$$Dye + OH^\bullet \rightarrow Degradation \tag{6}$$

Conclusion

The "unused" materials coated on the wall of the deposition unit (ZF-W) is demonstrated to be promising, useful in desired applications and comparable with the standard sample prepared by conventional approach (ZF-S). The metal oxide composites of ZnO and α-Fe$_2$O$_3$ with different stoichiometry and oxygen defects are achieved by a very simple and cost-effective high-density DC thermal plasma process within a short period of time in a single growth process. In spite of having almost similar lattice parameters, same constituents, similar optical and magnetic properties and performances as active materials, ZF-W differs in many aspects from ZF-S as

(i) ZF-W is more crystalline with a lower concentration of defects (oxygen vacancy defect) compared to ZF-S.
(ii) Mossbauer spectra depicts the magnetite phase in the cubic spinel with the possibility of small amounts of Fe doped ZnO residue in the samples.
(iii) Better stoichiometry, higher conversion of α-Fe$_2$O$_3$ to Fe$_3$O$_4$ and hence relatively higher saturation magnetization, coercivity and remanence are evidenced from ZF-S.

(iv) With almost similar MB adsorption capacity, ZF-W shows better cycle stability than the ZF-S.

These anomalies are attributed to the variation in the composition and cationic distributions of the as-prepared samples (ZF-W and ZF-S). The variation in composition and cationic distributions is due to the different temperature during the deposition. This scalable and adaptable strategy to prepare metal oxide composite with two different intrinsic properties in the same production run is expected to offer practical feasibility for wastewater treatment and energy applications.

Declaration of Competing Interest

There are no conflict to declare.

CRediT authorship contribution statement

Boris Wareppam: Investigation, Formal analysis, Writing – original draft. **N. Joseph Singh:** Investigation, Formal analysis. **Soumee Chakraborty:** Investigation, Formal analysis, Writing – review & editing. **Ng. Aomoa:** Investigation. **M. Kakati:** Investigation. **A.C. de Oliveira:** Investigation, Formal analysis. **V.K. Garg:** Investigation, Formal analysis. **K. Priyananda Singh:** Formal analysis. **Suelen Barg:** Writing – review & editing. **Subrata Ghosh:** Supervision, Methodology, Visualization, Investigation, Writing – review & editing. **L. Herojit Singh:** Supervision, Conceptualization, Investigation, Funding acquisition, Writing – review & editing.

Supplementary materials

Supplementary material associated with this article can be found, in the online version, at doi:10.1016/j.ceja.2021.100120.

References

[1] E. Pomerantseva, F. Bonaccorso, X. Feng, Y. Cui, Y. Gogotsi, Energy storage: the future enabled by nanomaterials, Science (80-.). 366 (6468) (2019) eaan8285, doi:10.1126/science.aan8285.
[2] R. Gusain, K. Gupta, P. Joshi, O.P. Khatri, Adsorptive removal and photocatalytic degradation of organic pollutants using metal oxides and their composites: a comprehensive review, Adv. Colloid Interface Sci. 272 (2019) 102009, doi:10.1016/j.cis.2019.102009.
[3] S. Ghosh, S.R. Polaki, N. Kumar, S. Amirthapandian, M. Kamruddin, K. Ostrikov, Process-specific mechanisms of vertically oriented graphene growth in plasmas, Beilstein J. Nanotechnol. 8 (1) (2017) 1658–1670, doi:10.3762/bjnano.8.166.
[4] S. Ghosh, S.R. Polaki, N.G. Krishna, M. Kamruddin, Influence of nitrogen on the growth of vertical graphene nanosheets under plasma, J. Mater. Sci. 53 (10) (2018) 7316–7325, doi:10.1007/s10853-018-2080-3.
[5] S. Ghosh, K. Ganesan, S.R. Polaki, S. Ilango, S. Amirthapandian, S. Dhara, M. Kamruddin, A.K. Tyagi, Flipping growth orientation of nanographitic structures by plasma enhanced chemical vapor deposition, RSC Adv. 5 (111) (2015) 91922–91931, doi:10.1039/C5RA20820C.
[6] V. Kumar, J.H. Kim, C. Pendyala, B. Chernomordik, M.K. Sunkara, Gas-phase, bulk production of metal oxide nanowires and nanoparticles using a microwave plasma jet reactor, J. Phys. Chem. C 112 (46) (2008) 17750–17754, doi:10.1021/jp8078315.
[7] M. Kumar, Y. Ando, Chemical vapor deposition of carbon nanotubes: a review on growth mechanism and mass production, J. Nanosci. Nanotechnol. 10 (6) (2010) 3739–3758, doi:10.1166/jnn.2010.2939.
[8] Y. Cui, J. Cheng, Q. Chen, Z. Yin, The types of plasma reactors in wastewater treatment, IOP Conf. Ser. Earth Environ. Sci. (1) (2018) 208, doi:10.1088/1755-1315/208/1/012002.
[9] T. Wang, Y. Li, G. Qu, Q. Sun, D. Liang, S. Hu, L. Zhu, Enhanced removal of humic acid from micro-polluted source water in a surface discharge plasma system coupled with activated carbon, Environ. Sci. Pollut. Res. 24 (27) (2017) 21591–21600, doi:10.1007/s11356-017-9807-6.

[10] X. Tao, C. Sun, Y. Han, L. Huang, D. Xu, The plasma assisted preparation of Fe-MOFs with high adsorption capacity, CrystEngComm 21 (15) (2019) 2541–2550, doi:10.1039/C9CE00015A.

[11] N.J. Singh, B. Wareppam, S. Ghosh, B.P. Sahu, P.K. Ajikumar, P. Singh, S. Chakraborty, S.S. Pati, A.C. Oliveira, S. de Barg, V. Garg, H.S. Lousham-bam, Alkali-cation incorporated and functionalized iron oxide nanoparticles for methyl blue removal/decomposition, Nanotechnology (2020), doi:10.1088/1361-6528/ab9af1.

[12] B. Saha, S. Das, J. Saikia, G. Das, Preferential and enhanced adsorption of different dyes on iron oxide nanoparticles: a comparative study, J. Phys. Chem. C 115 (16) (2011) 8024–8033, doi:10.1021/jp109258f.

[13] S. Noreen, U. Khalid, S.M. Ibrahim, T. Javed, A. Ghani, S. Naz, M. Iqbal, ZnO, MgO and FeO adsorption efficiencies for direct sky blue dye: equilibrium, kinetics and thermodynamics studies, J. Mater. Res. Technol. 9 (3) (2020) 5881–5893, doi:10.1016/J.JMRT.2020.03.115.

[14] K.K. Kefeni, B.B. Mamba, T.A.M Msagati, Application of spinel ferrite nanoparticles in water and wastewater treatment: a review, Sep. Purif. Technol. (2017) 399–422 Elsevier B.V., doi:10.1016/j.seppur.2017.07.015.

[15] J.P. Dhal, B.G. Mishra, G. Hota, Hydrothermal synthesis and enhanced photocatalytic activity of ternary $Fe_2O_3/ZnFe_2O_4/ZnO$ nanocomposite through cascade electron transfer, RSC Adv. 5 (71) (2015) 58072–58083, doi:10.1039/c5ra05894e.

[16] G. Yi, G. Agarwal, Y. Zhang, ZnO nanocrystal coated zinc particles degrade dyes in the dark by constantly releasing $\bullet O_2^-$ and H_2O_2, J. Phys. Chem. C 123 (31) (2019) 19230–19237, doi:10.1021/acs.jpcc.9b05393.

[17] B. Bora, N. Aomoa, M. Kakati, Characteristics and temperature measurement of a non-transferred cascaded DC plasma torch, Plasma Sci. Technol. 12 (2) (2010) 181–187, doi:10.1088/1009-0630/12/2/11.

[18] S. Kunj, K. Sreenivas, Residual stress and defect content in magnetron sputtered ZnO films grown on unheated glass substrates, Curr. Appl. Phys. 16 (7) (2016) 748–756, doi:10.1016/j.cap.2016.04.008.

[19] A. Roychowdhury, S.P. Pati, A.K. Mishra, S. Kumar, D. Das, Magnetically addressable fluorescent Fe_3O_4/ZnO nanocomposites: structural, optical and magnetization studies, J. Phys. Chem. Solids 74 (6) (2013) 811–818, doi:10.1016/j.jpcs.2013.01.012.

[20] Ling; Y.; Wheeler; D.A.; Zhang, J.Z.; Li, Y. Optical properties and applications of hematite (; 2013; Vol. 8.

[21] S. Kunj, K. Sreenivas, Defect mediated ferromagnetism in cluster free $Zn_{1-x}NixO$ nanopowders prepared by combustion method, J. Ind. Eng. Chem. 60 (2018) 151–159, doi:10.1016/j.jiec.2017.10.051.

[22] H. Chen, J. Ding, W. Guo, G. Chen, S. Ma, Blue-green emission mechanism and spectral shift of Al-doped ZnO films related to defect levels, RSC Adv. 3 (30) (2013) 12327–12333, doi:10.1039/c3ra40750k.

[23] S.S. Kostina, J.A. Peters, W. Lin, P. Chen, Z. Liu, P.L. Wang, Photoluminescence fatigue and inhomogeneous line broadening in semi- insulating Tl 6 SeI 4 single crystals, Semicond. Sci. Technol. 31 (6) (2016) 1–10, doi:10.1088/0268-1242/31/6/065009.

[24] J. Liqiang, Q. Yichun, W. Baiqi, L. Shudan, J. Baojiang, Y. Libin, F. Wei, F. Honggang, S. Jiazhong, Review of photoluminescence performance of nano-sized semiconductor materials and its relationships with photocatalytic activity, Sol. Energy Mater. Sol. Cells 90 (12) (2006) 1773–1787, doi:10.1016/j.solmat.2005.11.007.

[25] J. Liqiang, S. Xiaojun, X. Baifu, W. Baiqi, C. Weimin, F. Honggang, The preparation and characterization of La doped TiO_2 nanoparticles and their photocatalytic activity, J. Solid State Chem. 177 (10) (2004) 3375–3382, doi:10.1016/j.jssc.2004.05.064.

[26] S. Kumar, S. Mukherjee, R. Kr. Singh, S. Chatterjee, A.K Ghosh, Structural and optical properties of sol-gel derived nanocrystalline Fe-doped ZnO, J. Appl. Phys. (10) (2011) 110, doi:10.1063/1.3658221.

[27] A. Sahai, Y. Kumar, V. Agarwal, S.F. Olive-Méndez, N. Goswami, Doping concentration driven morphological evolution of Fe doped ZnO nanostructures, J. Appl. Phys. (16) (2014) 116, doi:10.1063/1.4900721.

[28] R. Gupta, A.K. Sood, P. Metcalf, J.M. Honig, Raman study of stoichiometric and Zn-doped Fe_3O_4, Phys. Rev. B Condens. Matter Mater. Phys. 65 (10) (2002) 1044301–1044308, doi:10.1103/PhysRevB.65.104430.

[29] N. Romčević, R. Kostić, M. Romčević, B. Hadžić, I. Kuryliszyn-Kudelska, W. Dobrowolski, U. Narkiewicz, D. Sibera, Raman scattering from ZnO(Fe) nanopar tides, Acta Phys. Pol. A 114 (5) (2008) 1323–1328, doi:10.12693/APhysPolA.114.1323.

[30] Z. Wang, D. Schiferl, Y. Zhao, H.S.C O'Neill, High pressure Raman spectroscopy of spinel-type ferrite $ZnFe_2O_4$, J. Phys. Chem. Solids 64 (12) (2003) 2517–2523, doi:10.1016/j.jpcs.2003.08.005.

[31] Z. Mao, W. Song, X. Xue, W. Ji, L. Chen, J.R. Lombardi, B. Zhao, Multiphonon resonant Raman scattering and photoinduced charge-transfer effects at ZnO-molecule interfaces, J. Phys. Chem. C 116 (51) (2012) 26908–26918, doi:10.1021/jp3092573.

[32] R. Cuscó, E. Alarcón-Lladó, J. Ibáñez, L. Artús, J. Jiménez, B. Wang, M.J. Callahan, Temperature dependence of Raman scattering in ZnO, Phys. Rev. B Condens. Matter Mater. Phys. 75 (16) (2007) 1–11, doi:10.1103/PhysRevB.75.165202.

[33] R. Sánchez Zeferino, M. Barboza Flores, U. Pal, Photoluminescence and Raman scattering in Ag-doped Zno nanoparticles, J. Appl. Phys. (1) (2011) 109, doi:10.1063/1.3530631.

[34] I. Chamritski, G. Burns, Infrared- and Raman-active phonons of magnetite, maghemite, and hematite: a computer simulation and spectroscopic study, J. Phys. Chem. B 109 (11) (2005) 4965–4968, doi:10.1021/jp048748h.

[35] D. Zhang, W. Choi, Y. Oshima, U. Wiedwald, S.H. Cho, H.P. Lin, Y.K. Li, Y. Ito, K. Sugioka, Magnetic Fe@FeOx, Fe@C and α-Fe$_2$O$_3$ single-crystal nanoblends synthesized by femtosecond laser ablation of Fe in acetone, Nanomaterials 8 (8) (2018), doi:10.3390/nano8080631.

[36] L.I. Granone, A.C. Ulpe, L. Robben, S. Klimke, M. Jahns, F. Renz, T.M. Gesing, T. Bredow, R. Dillert, D.W. Bahnemann, Effect of the degree of inversion on optical properties of spinel $ZnFe_2O_4$, Phys. Chem. Chem. Phys. 20 (44) (2018) 28267–28278, doi:10.1039/c8cp05061a.

[37] A. Serrano, J.F. Fernández, O. Rodríguez de la Fuente, M.A. García, A novel route to obtain metal and oxide nanoparticles co-existing on a substrate, Mater. Today Chem. 4 (September) (2017) 64–72, doi:10.1016/j.mtchem.2017.02.005.

[38] P. Dhiman, S. Sharma, A. Kumar, M. Shekh, G. Sharma, M. Naushad, Rapid visible and solar photocatalytic Cr(VI) reduction and electrochemical sensing of dopamine using solution combustion synthesized $ZnO–Fe_2O_3$ nano heterojunctions: mechanism elucidation, Ceram. Int. 46 (8) (2020) 12255–12268, doi:10.1016/j.ceramint.2020.01.275.

[39] C. Karunakaran, P. Vinayagamoorthy, Superparamagnetic core/shell Fe_2O_3/ZnO nanosheets as photocatalyst cum bactericide, Catal. Today 284 (2017) 114–120, doi:10.1016/j.cattod.2016.11.022.

[40] A.M. Jubb, H.C. Allen, Vibrational spectroscopic characterization of hematite, maghemite, and magnetite thin films produced by vapor deposition, ACS Appl. Mater. Interfaces 2 (10) (2010) 2804–2812, doi:10.1021/am1004943.

[41] A. Lassoued, B. Dkhil, A. Gadri, S. Ammar, Control of the shape and size of iron oxide (α-Fe_2O_3) nanoparticles synthesized through the chemical precipitation method, Results Phys. 7 (2017) 3007–3015, doi:10.1016/j.rinp.2017.07.066.

[42] P. Kumar, H. No-Lee, R. Kumar, Synthesis of phase pure iron oxide polymorphs thin films and their enhanced magnetic properties, J. Mater. Sci. Mater. Electron. 25 (10) (2014) 4553–4561, doi:10.1007/s10854-014-2203-9.

[43] N.M. Abdul Rashid, C. Haw, W. Chiu, N.H. Khanis, A. Rohaizad, P. Khiew, S. Abdul Rahman, Structural- and optical-properties analysis of single crystalline hematite (α-Fe_2O_3) nanocubes prepared by one-pot hydrothermal approach, CrystEngComm 18 (25) (2016) 4720–4732, doi:10.1039/c6ce00573j.

[44] Ogale, S.B.Dilute doping, defects, and ferromagnetism in metal oxide systems; 2010; Vol. 22. doi:10.1002/adma.200903891.

[45] P. Esquinazi, W. Hergert, D. Spemann, A. Setzer, A. Ernst, Defect-induced magnetism in solids, IEEE Trans. Magn. 49 (8) (2013) 4668–4674, doi:10.1109/TMAG.2013.2255867.

[46] B. Lesiak, N. Rangam, P. Jiricek, I. Gordeev, J. Tóth, L. Kövér, M. Mohai, P. Borowicz, Surface study of Fe_3O_4 nanoparticles functionalized with biocompatible adsorbed molecules, Front. Chem. 7 (October) (2019), doi:10.3389/fchem.2019.00642.

[47] A. Akbar, S. Riaz, M. Bashir, S. Naseem, Effect of Fe_{3+}/Fe_{2+} ratio on superparamagnetic behavior, IEEE Trans. Magn. 50 (8) (2014) 2–5.

[48] L.H. Singh, R. Govindaraj, G. Amarendra, C.S. Sundar, Point defects aspect of magnetite nano particles as studied by mossbauer spectroscopy, AIP Conf. Proc. 1447 (1) (2012) 445–446, doi:10.1063/1.4710071.

[49] F.S. Li, L. Wang, J.B. Wang, Q.G. Zhou, X.Z. Zhou, H.P. Kunkel, G. Williams, Site preference of Fe in nanoparticles of $ZnFe_2O_4$, J. Magn. Magn. Mater. 268 (3) (2004) 332–339, doi:10.1016/S0304-8853(03)00544-4.

[50] J.J. Beltrán, C.A. Barrero, A. Punnoose, Understanding the role of iron in the magnetism of Fe doped ZnO nanoparticles, Phys. Chem. Chem. Phys. 17 (23) (2015) 15284–15296, doi:10.1039/c5cp01408e.

[51] M. Amir, H. Gungunes, A. Baykal, M.A. Almessiere, H. Sözeri, I. Ercan, M. Sertkol, S. Asiri, A. Manikandan, Effect of annealing temperature on magnetic and Mössbauer properties of $ZnFe_2O_4$ nanoparticles by Sol-Gel approach, J. Supercond. Nov. Magn. 31 (10) (2018) 3347–3356, doi:10.1007/s10948-018-4610-2.

[52] L.H. Singh, R. Govindaraj, G. Amarendra, C.S. Sundar, Partial inversion in nano zinc ferrite as studied using Mossbauer spectroscopy, AIP Conf. Proc. 1512 (2013) 322–323, doi:10.1063/1.4791041.

[53] D. Zu, H. Wang, S. Lin, G. Ou, H. Wei, S. Sun, H. Wu, Oxygen-deficient metal oxides: synthesis routes and applications in energy and environment, Nano Res. 12 (9) (2019) 2150–2163, doi:10.1007/s12274-019-2377-9.

[54] T. Yu, Z.X. Shen, Y. Shi, J. Ding, Cation migration and magnetic ordering in spinel $CoFe_2O_4$ powder: micro-Raman scattering study, J. Phys. Condens. Matter (37) (2002) 14, doi:10.1088/0953-8984/14/37/101.

[55] R. Ullah, J. Dutta, Photocatalytic degradation of organic dyes with manganese-doped ZnO nanoparticles, J. Hazard. Mater. 156 (1–3) (2008) 194–200, doi:10.1016/j.jhazmat.2007.12.033.

[56] P. Goyal, S. Chakraborty, S.K. Misra, Multifunctional Fe_3O_4-ZnO nanocomposites for environmental remediation applications, Environ. Nanotechnol. Monit. Manag. 10 (March) (2018) 28–35, doi:10.1016/j.enmm.2018.03.003.

[57] X. Zhang, J. Qin, Y. Xue, P. Yu, B. Zhang, L. Wang, R. Liu, Effect of aspect ratio and surface defects on the photocatalytic activity of ZnO nanorods, Sci. Rep 4 (2014) 4–11, doi:10.1038/srep04596.

[58] G.S. Parkinson, Z. Novotný, P. Jacobson, M. Schmid, U. Diebold, Room temperature water splitting at the surface of magnetite, J. Am. Chem. Soc. 133 (32) (2011) 12650–12655, doi:10.1021/ja203432e.

[59] X. Wang, W. Yang, Y. Ji, X. Yin, Y. Liu, X. Liu, F. Zhang, B. Chen, N. Yang, Heterogeneous Fenton-like degradation of methyl blue using MCM-41-Fe/Al supported Mn oxides, RSC Adv. 6 (31) (2016) 26155–26162, doi:10.1039/c6ra04709b.

[60] X.L. Hao, L.Y. Zou, G.S. Zhang, Y.B. Zhang, Magnetic field assisted fenton reactions for the enhanced degradation of methyl blue, Chin. Chem. Lett. 20 (1) (2009) 99–101, doi:10.1016/j.cclet.2008.09.058.